Transition Metal Chemistry
https://doi.org/10.1007/s11243-021-00452-w

Investigation of the crystal structures and magnetic features of two bis(dithiolato)nickelate salts with flexible organic cations

Xuan-Rong Chen[1] · Zhen-Min Zhang[1] · Min Luo[1] · Hang Liu[1] · Jia-Yi Yuan[1]

Received: 4 December 2020 / Accepted: 24 February 2021
© The Author(s), under exclusive licence to Springer Nature Switzerland AG 2021

Abstract

Two bis(dithiolato)nickel salts with different flexible ammonium counterions, $[Et_3MeN][Ni(dmit)_2]$ (**1**) and $[(i\text{-}Bu)Et_3N][Ni(dmit)_2]$ (**2**) ($dmit^{2-}$ = 2-thioxo-1,3-dithiole-4,5-dithiolate, Et_3MeN^+ = triethylmethylammonium, $(i\text{-}Bu)Et_3N^+$ = triethylisobutylammonium), are prepared and identified by powder X-ray diffraction (PXRD) patterns and single-crystal X-ray diffraction. Salt **1** crystallizes in the triclinic space group $P-1$ at 293 K. The anions and cations in **1** form alternating layered arrangements along the *a*-axis direction. Salt **2** belongs to the monoclinic crystal system and space group $P2_1/n$. The anions and cations in **2** form separate columnar stacks along *bc*-plane direction. The neighboring anions are stacked as dimers in the anion columnar stacks of **2**. The magnetic features of salts **1** and **2** show 1D alternating spin chain magnetic exchange behavior, and the magnetic experimental data are well fitted through a spin chain magnetic model. The difference in the crystal structures and magnetic properties between the two new salts **1** and **2** fully demonstrates that the magnetic properties are dependent on the alignment of the $[Ni(dmit)_2]^-$ anions, which are related to the flexible organic cations.

Introduction

Metal bis-1,2-dithiolene complexes have been increasingly studied in recent decades [1–7]. In recent years, some novel properties, such as ion conductivity and dielectric properties, have been found in these complexes [8–13]. Planar $[M(dithiolate)_2]^-$ monoanions are easily aligned into columnar stacks to form a 1D magnetic chain with spin–lattice interactions between neighboring anions. Therefore, spin-Peierls-type magnetic behavior is commonly observed and has been reported in many bis(dithiolate) metal complexes [14–20].

$[M(dmit)_2]^-$ complexes are well-known metal bis-1,2-dithiolene complexes with unusual magnetic properties and conducting properties [21–33]. Investigations on $[M(dmit)_2]^-$ complexes have focused on obtaining unusual physicochemical properties by introducing appropriate cations. First, Nakamura's group [34–41] reported an interesting $[Ni(dmit)_2]^-$ system by introducing a metal crown ether cation, with the system showing novel magnetic and conducting properties and ferroelectricity. Some researchers have introduced Fe^{II} or Mn^{III} cations with spin crossover behavior into the $[Ni(dmit)_2]^-$ system to obtain novel molecular magnets with spin transition and magnetic bistability [42–51]. In addition, ammonium organic cations can be introduced into the $[M(dmit)_2]$ system to obtain a series of molecular conductors, and their crystal structures and electrical properties have been intensively investigated in reported research papers [52–56]. However, the magnetic properties of these molecular conductors with ammonium cations as counterions have rarely been studied. The $[M(dmit)_2]^-$ salts usually show structural phase transitions in their high-temperature phase (HTP) and in low-temperature phase (LTP) due to the disorder–order transitions of ammonium cations, accordingly exhibiting magnetic phase transitions due to

✉ Xuan-Rong Chen
chenxr@yctu.edu.cn

Zhen-Min Zhang
2031264406@qq.com

Min Luo
1002951937@qq.com

Hang Liu
1830080690@qq.com

Jia-Yi Yuan
2587457343@qq.com

[1] School of Chemistry and Environmental Engineering and Instrumental Analysis Center, Yancheng Teachers University, 2# Xiwang Road, Yancheng 224007, People's Republic of China

Published online: 12 March 2021

the disorder–order transitions of the organic cations and the structural phase transitions of the complexes.

In previous studies, our group focused on investigating $[Ni(dmit)_2]^-$ salts by incorporating flexible organic cations as counterions, such as pyridinium cations [57–59], imidazole cations and ammonium cations. Recently, we achieved a bis(dithiolate)nickel salt $[Et_3(n\text{-}Pr)N][Ni(dmit)_2]$ [60], which showed a magnetic transition with large thermal hysteresis. This magnetic transition resulted from a structural phase transition with a lattice symmetry increase from HTP to LTP.

To expand the research on $[Ni(dmit)_2]^-$ salts, we chose more flexible organic cations for use with the $[Ni(dmit)_2]^-$ building blocks to obtain novel molecular solids with magnetic features. In this paper, we present the crystal structures and magnetic features of two new salts, $[Ni(dmit)_2]^-$ with triethylmethylammonium and triethylisobutylammonium.

Experimental

Materials

All AR chemicals were used without further purification. 4,5-Di(thiobenzoyl)-1,3-dithiole-2-thione ($dmit(COPh)_2$) [61] and $(Et_3MeN)Cl$, $[(i\text{-}Bu)Et_3N]Br$ [62] were prepared according to the published method.

Preparation of $[Et_3MeN][Ni(dmit)_2]$ (1)

Sodium methoxide was prepared by placing 210 mg of sodium metal in 20 mL of methanol, and then this sodium methoxide was dropwise added into a methanol (20 mL) solution of $dmit(COPh)_2$ (815 mg, 2 mmol) in a nitrogen atmosphere at room temperature. After stirring for 30 min, the mixture gradually became a dark red solution. Then, $NiCl_2{\cdot}6H_2O$ (240 mg, 1 mmol), $(Et_3MeN)Cl$ (162 mg, 1 mmol) and I_2 (128 mg, 0.5 mmol) were added to the above mixed solution, producing a dark green precipitate after approximately 2 h. The dark green precipitate was collected by vacuum filtration, washed with methanol and dried in vacuum. Yield: 70%. Anal. Calc. for $C_{13}H_{18}NNiS_{10}$: C, 27.51; N, 2.47; H, 3.20%. Found: C, 27.09; N, 2.21; H, 3.16%. IR bands (KBr pellet, cm^{-1}) [63]: 1349($\nu_{C=C}$), 1057($\nu_{C=S}$).

Preparation of $[(i\text{-}Bu)Et_3N][Ni(dmit)_2]$ (2)

A procedure similar to **1** was used for the preparation of $[(i\text{-}Bu)Et_3N][Ni(dmit)_2]$ (**2**), but instead of $[Et_3MeN]Cl$, $[(i\text{-}Bu)Et_3N]Br$ (152 mg, 1 mmol) was used. Yield: 75%. Anal. Calc. for $C_{16}H_{24}NNiS_{10}$: C, 31.52; N, 2.30; H, 3.97%. Found: C, 31.51; N, 2.25; H, 3.93%. IR bands (KBr pellet, cm^{-1}) [63]: 1342 ($\nu_{C=C}$), 1058($\nu_{C=S}$).

Single crystals were obtained through by slowly evaporating of the acetone solution of powdered samples of **1** and **2** at ambient temperature for 7 – 14 days. The phase purities of **1** and **2** were determined through their PXRD patterns, and the experimental and simulated XRD patterns were consistent, as displayed in Figs. S4 and S5.

Physical measurements

C, H and N elemental analyses were performed on a PerkinElmer 2400 II Elementar Vario analytic instrument. IR spectra of **1** and **2** were recorded from 4000 to 400 cm^{-1} on a Bruker Vertex 80 Fourier Transform Infrared Spectrometer after mixing the powdered samples with solid KBr. PXRD data were collected on a Bruker D8 diffractometer with a Cu Kα radiation source ($\lambda = 1.5418$ Å) with a scanning range of 5 to 50° and a scanning rate of 2° min^{-1}. Thermogravimetric analyses of the powdered samples of **1** and **2** were performed on a NETZSCH STA 449F5 thermogravimetric analyzer, and the samples (~5 mg for **1** and **2**) were placed in an Al_2O_3 crucible for heating from 30 to 800 °C. Magnetic property measurements of **1** and **2** were collected with a Quantum Design MPMS-XL superconducting quantum interference device (SQUID) magnetometer using powdered samples (~60 mg) from 1.8 to 400 K under a magnetic field of 10,000 Oe.

Refinement X-ray crystallography

Single crystals of **1** and **2** were selected and mounted on a glass capillary, and diffraction intensity data were collected at 293 and 100 K by a Bruker AXS SMART diffractometer equipped with a CCD area detector and Mo Kα ($\lambda = 0.71073$ Å) radiation [64, 65]. The structures of **1** and **2** were solved using the direct method and refined with the SHELX-2014 [66] by the full-matrix least-squares procedure on F^2. All nonhydrogen atoms were anisotropically refined, and hydrogen atoms were introduced at calculated positions. The crystallographic details of the data collection and structure refinements of **1** and **2** at 293 K and 100 K are summarized in Table 1 and Table 2.

Calculation of overlap integral within anion–anion pairs

The intermolecular overlap integrals were calculated for two neighboring $[Ni(dmit)_2]$ anions (considered as a dimer) using Multiwfn program [67], and the SOMO of each $[Ni(dmit)_2]$ anion in the selected dimer was used as the basis function for the calculation of intermolecular overlap integrals, which is obtained by DFT calculation using the

Table 1 Crystallographic data and structural refinement data of **1** and **2** at 293 K

Compound	**1**	**2**
Temperature (K)	293	293
Chemical formula	$C_{13}H_{18}NNiS_{10}$	$C_{16}H_{24}NNiS_{10}$
Formula weight	567.59	609.65
Wavelength (Å)	0.71073	0.71073
CCDC numbers	2,023,007	2,023,008
Crystal system	Triclinic	Monoclinic
Space group	$P-1$	$P2_1/n$
a (Å)	7.4366(8)	8.3368(15)
b (Å)	12.4959(13)	27.159(5)
c (Å)	12.5215(12)	11.782(2)
α (°)	90.255(3)	90
β (°)	98.229(3)	102.293(5)
γ (°)	102.877(3)	90
V (Å^3)/Z	1121.8(2)/2	2606.6(8)/4
ρ (g×cm^{-3})	1.680	1.554
F (000)	582	1682
Abs. coeff. (mm^{-1})	1.795	1.551
θ Ranges (data collection°)	1.67–27.51	2.84–27.56
Index range	$-8 \le h \le 9$	$-10 \le h \le 10$
	$-16 \le k \le 16$	$-35 \le k \le 35$
	$-14 \le l \le 16$	$-15 \le l \le 15$
R_{int}	0.0398	0.0331
Independent reflections/ restraints/parameters	5128/0/230	6001/0/258
Refined method	Full-matrix least-squares on F^2	
Goodness of fit on F^2	1.099	1.028
R_1, wR_2 [$I > 2\sigma(I)$]	$R_1 = 0.0355$	$R_1 = 0.0379$
	$wR_2 = 0.0875$	$wR_2 = 0.0799$
R_1, wR_2 [all data]	$R_1 = 0.0481$	$R_1 = 0.0613$
	$wR_2 = 0.0936$	$wR_2 = 0.0888$
Residual (e nm^{-3})	0.508/− 0.749	0.537/− 0.343

$R_1 = \Sigma(|F_o| - |F_c|)/\Sigma|F_o|$,
$wR_2 = \Sigma w\left[\left(|F_o|^2 - |F_c|^2\right)^2/\Sigma w\left(|F_o|^2\right)^2\right]^{1/2}$

Table 2 Crystallographic data and structural refinement data of **1** and **2** at 100 K

Compound	**1**	**2**
Temperature (K)	100	100
Chemical formula	$C_{13}H_{18}NNiS_{10}$	$C_{16}H_{24}NNiS_{10}$
Formula weight	567.59	609.65
Wavelength (Å)	0.71073	0.71073
CCDC numbers	2,063,630	2,063,631
Crystal system	Triclinic	Monoclinic
Space group	$P-1$	$P2_1/n$
a (Å)	7.2683(11)	8.2469(2)
b (Å)	12.3593(19)	27.5517(5)
c (Å)	12.6112(19)	11.3808(2)
α (°)	89.814(4)	90
β (°)	97.765(4)	101.674(2)
γ (°)	103.634(4)	90
V (Å^3)/Z	1090.4(3)/2	2532.41(9)/4
ρ (g×cm^{-3})	1.729	1.599
F (000)	582	1260
Abs. coeff. (mm^{-1})	1.847	1.597
θ Ranges (data collection°)	2.912–27.635	1.478–30.172
Index range	$-9 \le h \le 9$	$-11 \le h \le 10$
	$-16 \le k \le 16$	$-37 \le k \le 36$
	$-16 \le l \le 16$	$-15 \le l \le 14$
R_{int}	0.0480	0.0424
Independent reflections/ restraints/parameters	4880/6/230	6544/0/258
Refined method	Full-matrix least-squares on F^2	
Goodness of fit on F^2	1.204	1.052
R_1, wR_2 [$I > 2\sigma(I)$]	$R_1 = 0.0758$	$R_1 = 0.0304$
	$wR_2 = 0.2106$	$wR_2 = 0.0702$
R_1, wR_2 [all data]	$R_1 = 0.0798$	$R_1 = 0.0407$
	$wR_2 = 0.2123$	$wR_2 = 0.0741$
Residual (e nm^{-3})	1.997/− 1.014	0.553/− 0.350

$R_1 = \Sigma(|F_o| - |F_c|)/\Sigma|F_o|$,
$wR_2 = \Sigma w\left[\left(|F_o|^2 - |F_c|^2\right)^2/\Sigma w\left(|F_o|^2\right)^2\right]^{1/2}$

basis set of B3LYP/6-31G* for C, N and S elements, the relativistic effective core potential basis set of lanl2dz for Ni element by Gaussian 09 program [68], and the default values of convergence criteria are set. Each dimer structure was extracted from the single crystal structure of **1** and **2** at 293 and 100 K.

Results and discussion

Crystal structures

1 crystallizes in the triclinic crystal system with space group $P-1$ at 293 K. As depicted in Fig. 1a, an asymmetric unit of **1** contains one $(Et_3MeN)^+$ cation and one $[Ni(dmit)_2]^-$ anion. The $[Ni(dmit)_2]^-$ anion is square planar, the Ni–S bond length is between 2.1518(6) and 2.1748(6) Å, and the oxidation state of nickel is 3^+. The bond distance and bond angles in the $[Ni(dmit)_2]^-$ moieties, listed in Table S1, are comparable to those in other reported $[Ni(dmit)_2]^-$ analogs [53–56]. The alkyl chain of $(Et_3MeN)^+$ cations is ordered at 293 K for **1**, and the bond length and angle values in the alkyl chains are comparable to those in other ammonium cations [48–52].

As shown in Fig. 1b, the anions and cations in **1** form an alternating chain arrangement along the a axis direction. The neighboring cations are arranged in centrosymmetric styles (Fig. 1c); there are only van der Waals forces

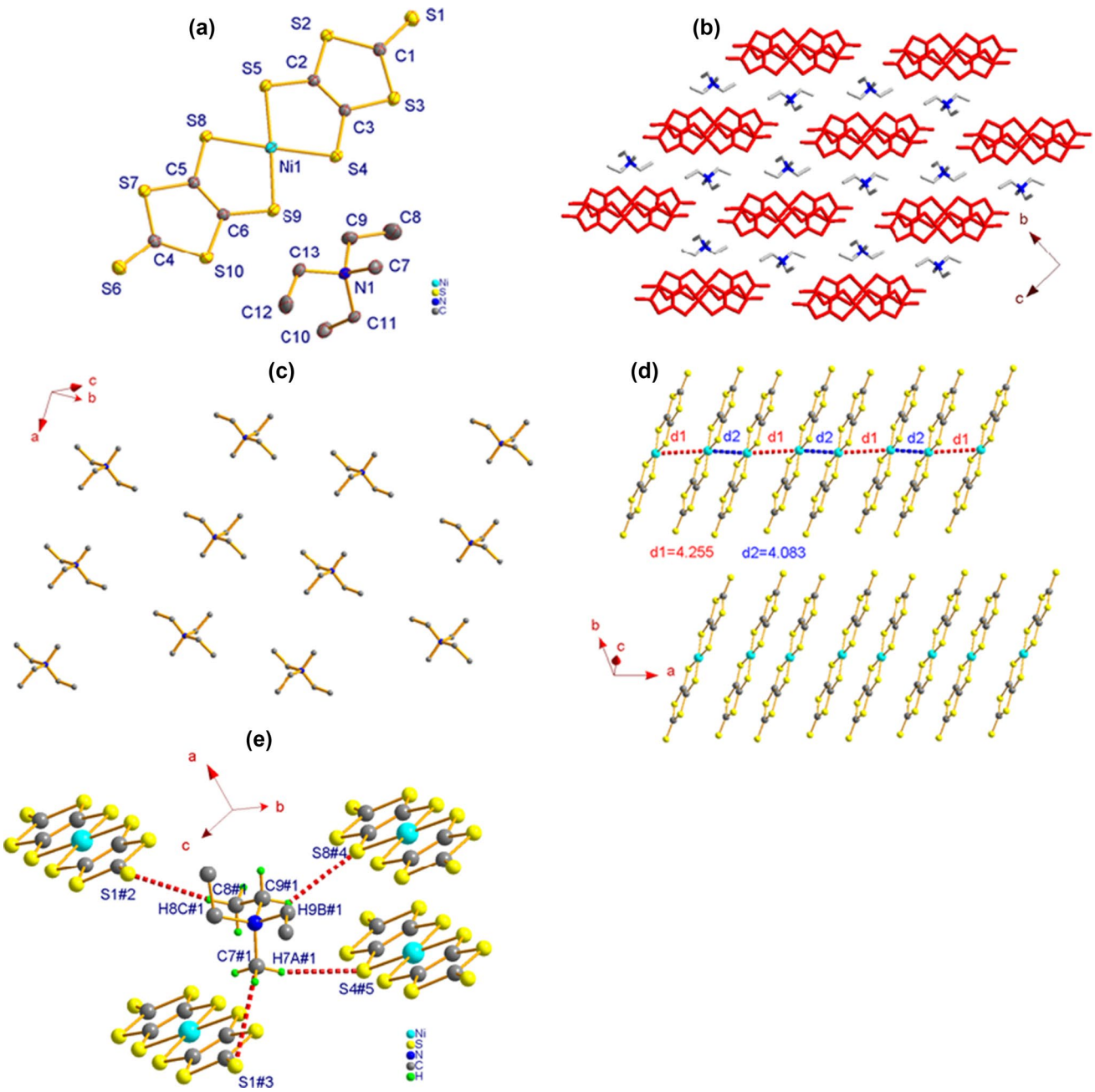

Fig. 1 **a** Molecular structure of **1** with displacement ellipsoids at a 20% probability level at 293 K (hydrogen atoms omitted for clarity); **b** packing diagram showing alternating layered arrangements of the anions and cations along the *a* axis direction (H atoms omitted for clarity) for **1** at 293 K; **c** cation layer; **d** anion layers, in which the Ni…Ni distance between the adjacent superimposed anions is irregular; and **e** charge-assisted H-bonds between the cations and anions

between the adjacent cations in the *a* layer. The anionic layer is constructed by π-type anion dimers, in which two anions are related to each other through an inversion center and stacked in transverse and longitudinal offset modes. In the anion columnar stacks, the Ni…Ni distance between the adjacent superimposed anions is irregular, $d_1 = 4.255$ and $d_2 = 4.083$ Å in an anion stack (ref. Figure 1d). There are no obvious S…S contacts between the neighboring dimers in the $[Ni(dmit)_2]^-$ anions. As displayed in Fig. 1e, charge-assisted H-bonds are formed between the cations and anions, with the distances $d_{C8\#1\text{-}H8C\#1\ldots S1\#2} = 2.9658(8)$, $d_{C9\#1\text{-}H9B\#1\ldots S8\#4} = 2.9417(7)$, $d_{C7\#1\ldots S1\#3} = 3.4767(26)$, $d_{C7\#1\text{-}H7A\#1\ldots S4\#5} = 2.9797(7)$ and the symmetry codes #1 = − 1 + *x*, *y*, − 1 + *z*, #2 = 1 − *x*, 1 − *y*, − *z*, #3 = − *x*, 1 − *y*, − *z*, #4 = − *x*, 1 − *y*, 1 − *z*, #5 = − 1 + *x*, *y*, − 1 + *z*, and

these interatomic distances are less than the sum of the van der Waals radii of an H (C) atom and S atom.

1 also crystallizes in the triclinic crystal system with space group $P-1$ at 100 K in the low-temperature phase. As depicted in Fig. 2a, an asymmetric unit of **1** also contains one $(Et_3MeN)^+$ cation and one $[Ni(dmit)_2]^-$ anion. The corresponding bond distance and bond angles in the $[Ni(dmit)_2]^-$moieties, listed in Table S1, are comparable to **1** at 293 K. As shown in Fig. 2b, the anions and cations in **1** form an alternating chain arrangement along the *a* axis direction. It is noted that the crystal structure at 100 K in the low-temperature phase is nearly similar to that at 293 K in the high-temperature phase.

2 crystallizes in the monoclinic crystal system with space group $P2_1/n$ at 293 K. The asymmetric unit of **2** is composed of one $[(i\text{-}Bu)Et_3N]^+$ cation and one $[Ni(dmit)_2]^-$ anion, as depicted in Fig. 3a. The $[Ni(dmit)_2]^-$ anion is square planar, the Ni–S bond length is between 2.1576(8) and 2.1719(8) Å, and the oxidation state of nickel is 3^+. The bond parameters of **2** listed in Table S2 are rather similar to those in **1**. As displayed in Fig. 3b, the anions and cations in **2** are arranged in the style of columnar stacks along the *a*-axis direction. The anions are arranged in two different styles, forming a zig-zag chain arrangement viewed along the $a+c$ direction (ref. Figure 4a). As depicted in Fig. 4b, c, the neighboring

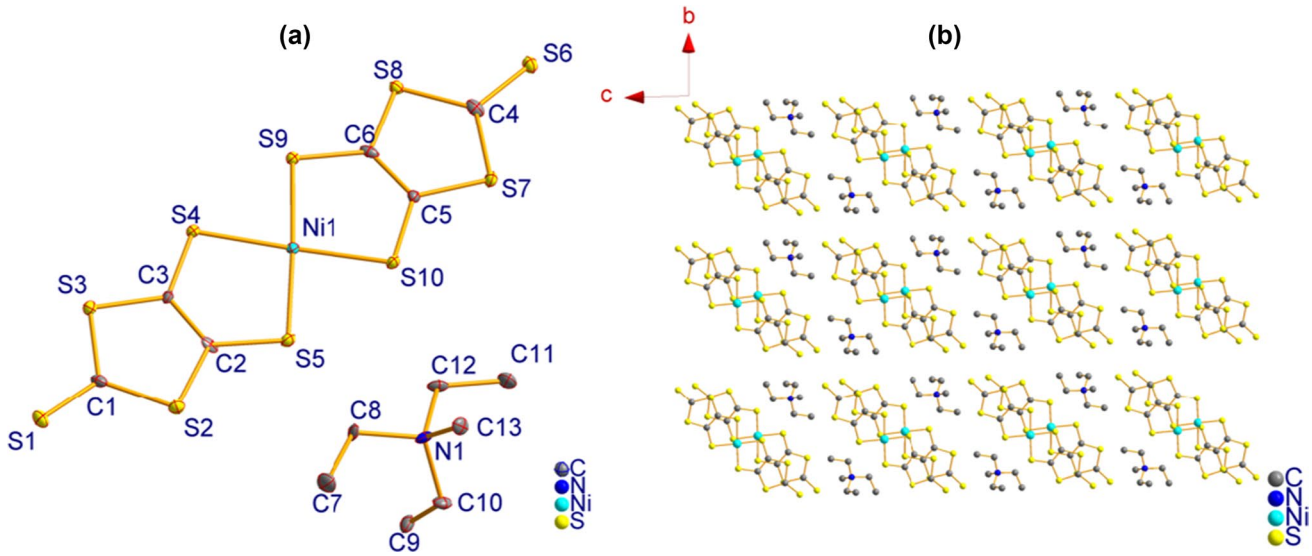

Fig. 2 **a** Molecular structure of **1** with displacement ellipsoids at a 50% probability level at 100 K (hydrogen atoms omitted for clarity); **b** packing diagram showing alternating layered arrangements of the anions and cations along the *a* axis direction for **1** at 100 K

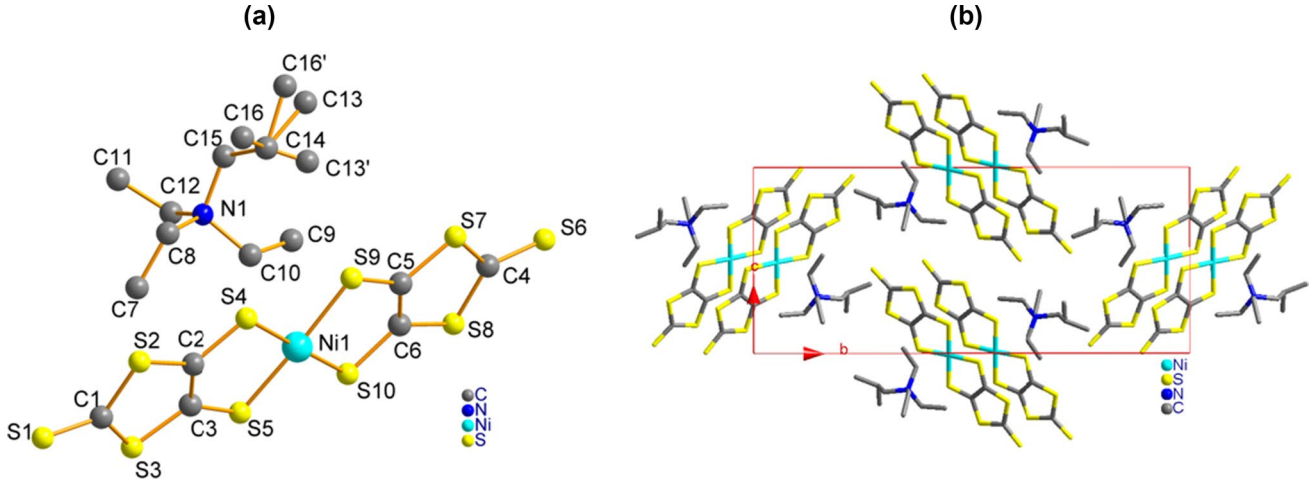

Fig. 3 **a** Asymmetric unit with thermal ellipsoids drawn at a 30% probability level for **2** at 293 K; **b** packing diagram showing the arrangement of separated columnar stacks along the *c*-axis direction of **2** at 293 K

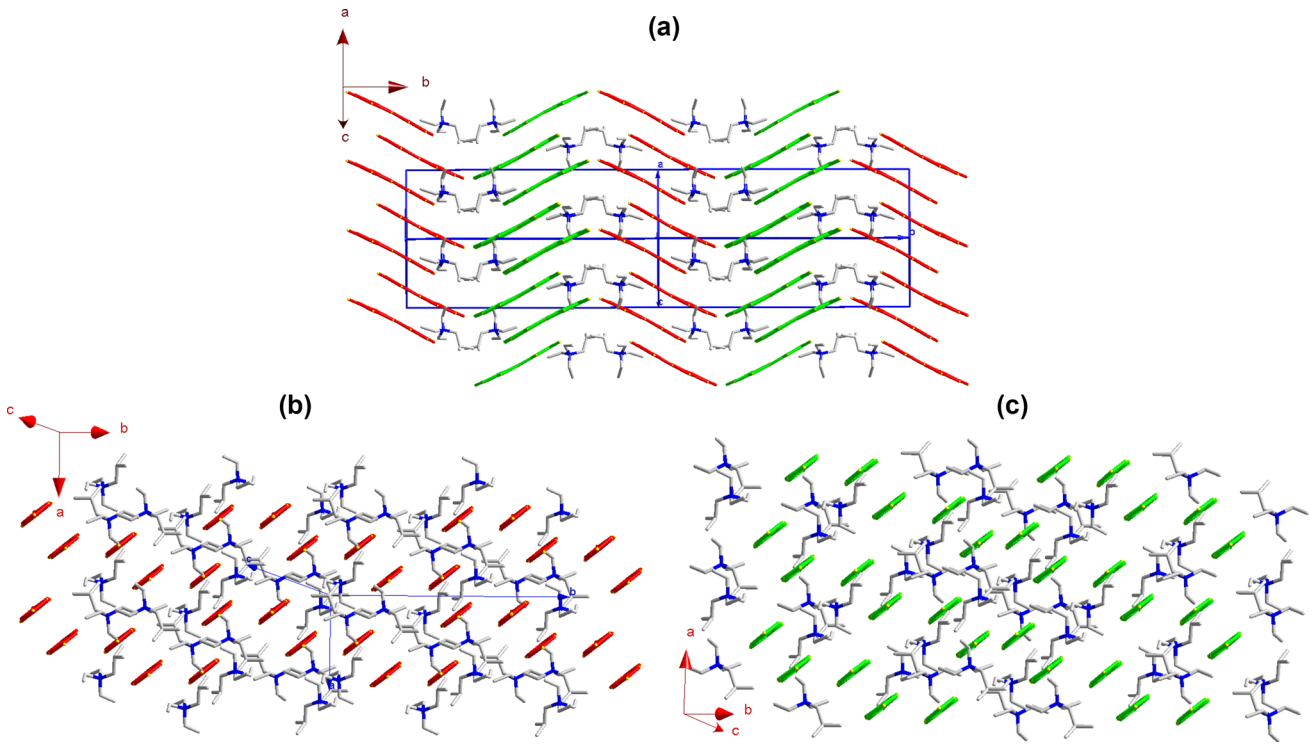

Fig. 4 **a** Anions in the manner of two different styles, forming a zigzag chain arrangement and the **b**, **c** neighboring anions stacked as dimers in the anion columnar stacks of **2** at 293 K

anions are stacked as dimers in the anion columnar stacks. There exist only short interatomic lateral S…S contacts between the anion columnar stacks, which are less than the sum of the van der Waals radii of two S atoms.

2 also crystallizes in the monoclinic crystal system with space group $P2_1/n$ at 100 K. The asymmetric unit of **2** is also composed of one $[(i\text{-}Bu)Et_3N]^+$ cation and one $[Ni(dmit)_2]^-$ anion, as depicted in Fig. 5a. The bond parameters of **2** at 100 K listed in Table S2 are rather similar to those in **2** at 293 K. As displayed in Fig. 5b, the anions and cations in **2** are arranged in the style of columnar stacks along the *a*-axis direction. It is noted that the crystal structure of **2** at 100 K in the low-temperature phase is also similar to that at 293 K in the high-temperature phase.

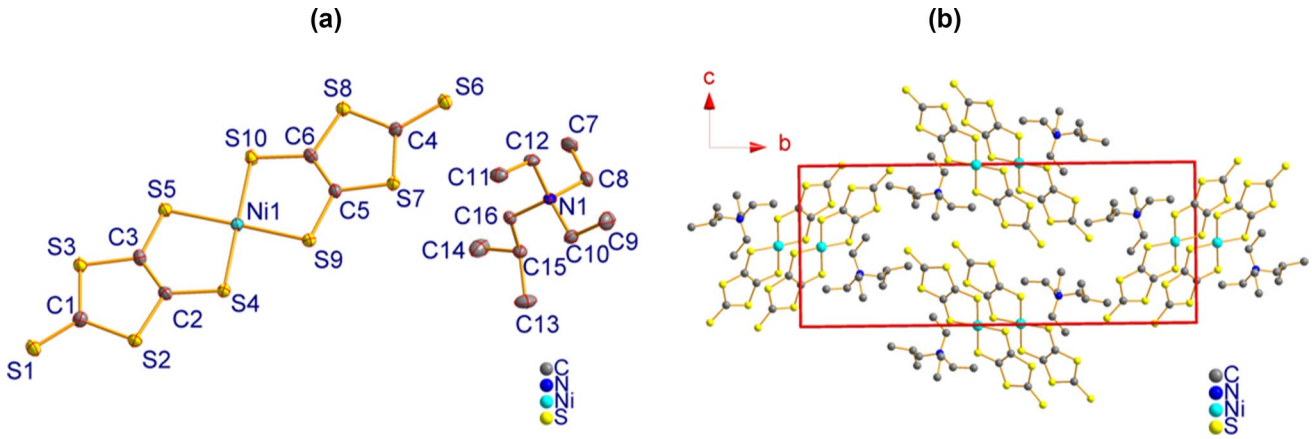

Fig. 5 **a** Asymmetric unit with thermal ellipsoids drawn at a 50% probability level for **2** at 100 K; **b** packing diagram showing the arrangement of separated columnar stacks along the *c*-axis direction of **2** at 100 K

Magnetic properties

In a spin system in which the magnetic behavior is dominated by AFM coupling, the magnetic exchange constant, J_{AF}, between two spins may be described as

$$J_{AF} \propto \frac{(2t)^2}{U_{eff}} \quad (1)$$

where the symbol t is the transfer integral between two spin sites, which is proportional to the overlap integral (S) of the interacting magnetic orbitals, and U_{eff} represents the effective on-site Coulomb repulsion and this is nearly constant for a defined magnetic solid. Consequently, the J_{AF} is directly proportional to S^2 of the interacting magnetic orbitals. As described in the section of the crystal structures of **1** and **2** at 293 K and 100 K, the crystal structures of **1** and **2** at 293 K are similar to those at 100 K. Furthermore, the [Ni(dmit)$_2$] anions in **1** and **2** form an alternating chain in the stacks, and AFM coupling is probably between the neighboring anions in the spin chain. Therefore, we calculated the overlap integral between the neighboring anions of **1** and **2** at 293 and 100 K. The calculated overlap integrals of anion–anion pairs are summarized in Table 3. The calculated overlap integral S^2 of Pair II at 293 K for **1** is 72.9, which is higher than 19.3 of Pair I, indicating a stronger AFM coupling between the neighboring anions of Pair II than Pair I. However, the calculated overlap integral S^2 of Pair II at 293 K for **2** is 99, near to 70.1 of Pair I, showing commensurate AFM coupling between the neighboring anions of Pair I and Pair II. Besides, the calculated overlap integral S^2 of Pair I and Pair II at 293 K is identical to those at 100 K for **1** and **2**, demonstrating that magnetic exchange interaction between the neighboring anions is almost similar in the low-temperature phase and in the high-temperature phase.

Table 3 The calculated overlap integral (S) and S^2 within anion–anion pairs at 293 and 100 K for **1** and **2**

1

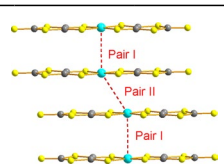

Temperature	293 K		100 K	
Anion–anion pairs	S (10^{-3})	S^2 (10^{-6})	S (10^{-3})	S^2 (10^{-6})
Pair I	− 4.39	19.3	− 4.60	21.2
Pair II	8.54	72.9	8.96	80.3

2

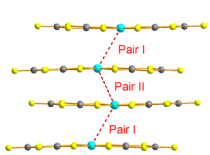

Temperature	293 K		100 K	
Anion–anion pairs	S (10^{-3})	S^2 (10^{-6})	S (10^{-3})	S^2 (10^{-6})
Pair I	8.37	70.1	8.76	76.7
Pair II	− 9.95	99.0	− 9.98	99.6

On the basis of the crystal structure analysis, a co-facial π-type dimer exists with two types of neighboring Ni⋯Ni distances in the anion column stacks for **1** and **2**, as a result, the salts **1** and **2** probably show the magnetic behavior of an $S = ½$ alternating spin chain in both phases. Consequently, an $S = ½$ antiferromagnetic (AFM) Heisenberg linear chain model was chosen for the analysis of magnetic susceptibility data of **1** and **2** in both phases. The spin Hamiltonian may be written as that in Eq. (2) for the Heisenberg alternating linear chain

$$\hat{H} = -2J \sum_{i=1}^{n/2} [\hat{S}_{2j-1}\hat{S}_{2j} + \alpha \hat{S}_{2j}\hat{S}_{2j+1}] \quad (2)$$

where J and αJ represent the exchange constants between a spin and its left neighbor, and between a spin and its right neighbor, respectively. For an AFM exchange system ($J < 0$ and $0 \le \alpha \le 1$), in the exteme, when $\alpha = 0$, the alternating linear chain model is simplified to the dimer model with pairwise interactions. When $\alpha = 1$ the alternating linear chain model reduces to the regular linear-chain model [69, 70]. Based on Eq. (3), the molar magnetic susceptibility as a function of temperature for an $S = ½$ Heisenberg antiferromagnetic linear chain, deduced from the cluster approach, can be expressed as

$$\chi_{chain} = \frac{Ng^2\mu_B^2}{k_B T} \cdot \frac{A + Bx + cx^2}{1 + Dx + Ex^2 + Fx^3} \quad (3)$$

where $x = |J|/k_B T$ and $J \le 0$. The Eq. (3) has two sets of parameters $A - F$ for the alternating-exchange linear spin chain [70]. The experimental molar magnetic susceptibility in both phases is given in Eq. (4) if the paramagnetic impurity, originating from the lattice defects, molecular diamagnetism of atoms core and the possible van Vleck-type temperature-independent paramagnetism, arising from the coupling of the ground and excited states through a magnetic field [69], are further considered.

$$\chi_m = \chi_{chain} + \frac{C}{T - \theta} + \chi_0 \quad (4)$$

The temperature-dependent magnetic susceptibility of **1** measured from 2 to 400 K in the cooling and heating process is displayed in Fig. 6, where the molar magnetic susceptibility data are processed through a diamagnetic correction using Pascal's constants [71]. In the $\chi_m - T$ plot of **1**, the compound shows a simple Curie–Weiss-type paramagnetic behavior in the low-temperature region (approximately

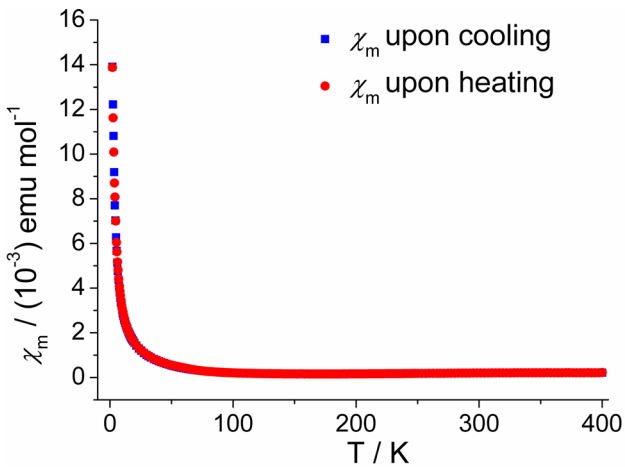

Fig. 6 Plots of χ_m versus T for **1** (the blue squares: experimental data of the magnetic susceptibility during the cooling process; red circles: experimental data of the magnetic susceptibility during the heating process). (Color figure online)

below 75 K). This type of paramagnetism is due to magnetic impurities, which originate from uncoupled spins of lattice defects.

As shown in Fig. 6, the χ_m values gradually increase as the temperature increases in the high-temperature region (above 150 K), showing the magnetic character of a Heisenberg alternating linear chain.

We used a 1D Heisenberg alternating spin chain magnetic model [Eq. (4)] to fit the temperature-dependent magnetic susceptibility of **1**. As displayed in Fig. 7, the variable temperature magnetic susceptibility from 1.8 to 400 K was fitted to Eq. (4), providing the following parameters for **1**: $\alpha = 0.22394$, $\Delta/k_B = 354.3$ K, $C = 0.03332$ emu·K·mol^{-1}, $\theta = -0.28943$ K, and $\chi_0 = -1.1 \times 10^{-4}$ emu·mol^{-1}, and the square of the correlation coefficient $R^2 = 0.996$ for **1**. The magnetic impurity from uncoupled $[Ni(dmit)_2]^-$ anions is estimated to be approximately 8.89% based on the fitted C value in **1**.

The $\chi_m - T$ plot of **2** from 2 to 300 K during the cooling process is displayed in Fig. 8, and the molar magnetic susceptibility data were processed similar to **1**. In the whole temperature region, the χ_m value reaches a maximum at ~ 175 K, and a large Curie–Weiss tail is also observed below ~ 50 K, indicating simple Curie–Weiss-type paramagnetism behavior due to magnetic impurities arising from lattice defects. Based on the crystal structure analysis, the anions and cations in **2** form columnar stacks along the a-axis direction. As a result, we used the 1D Heisenberg alternating spin chain magnetic model to analyze the magnetic behavior of **2**.

As shown in Fig. 8, the best fit is obtained for the magnetic susceptibility data from 2 to 300 K, providing the following parameters: $\alpha = 0.18115$, $J/k_B = 157.5$ K, $g = 1.91$, $C = 0.02524$ emu K mol^{-1}, $\theta = -2.9794$ K, and $\chi_0 = -5.7 \times 10^{-4}$ emu·mol^{-1}, and the square of the correlation coefficient $R^2 = 0.998$ for **2**. The magnetic impurity from uncoupled $[Ni(dmit)_2]^-$ anions is estimated to be approximately 6.73% based on the fitted C value in **2**.

Conclusions

In summary, two nickel-bis-1,2-dithiolene salts with different flexible ammonium organic cations, $[Et_3MeN][Ni(dmit)_2]$ (**1**) and $[(i\text{-}Bu)Et_3N][Ni(dmit)_2]$ (**2**), were synthesized and characterized by IR spectroscopy, PXRD and single-crystal X-ray diffraction. The two salts showed

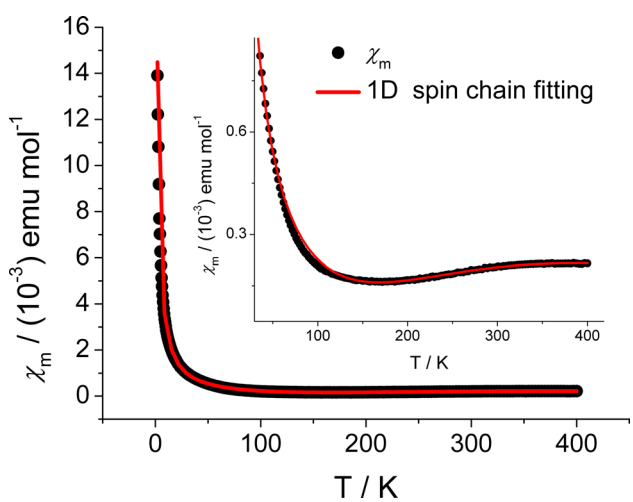

Fig. 7 Black circles are the experimental data of χ_m, and the red line represents the fit using the 1D Heisenberg alternating spin chain equation for **1**

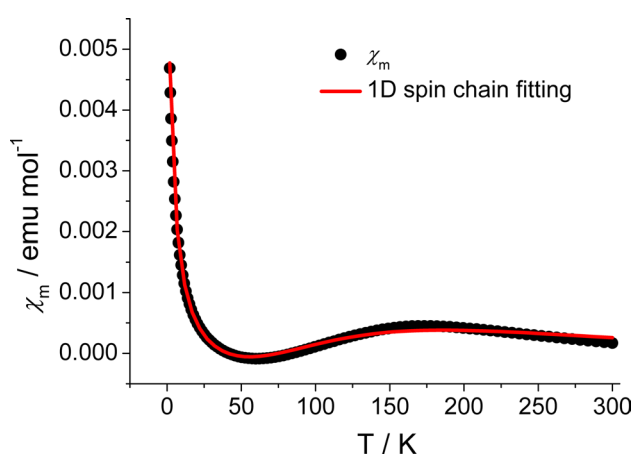

Fig. 8 Temperature-dependent χ_m of **2** from 2 to 300 K (the black circles are the experimental data, and the red line represents the fitting curve through the spin dimer fitting model). (Color figure online)

different crystal structures due to the geometric nature of the counterions in the crystals. **1** crystallized in the triclinic crystal system, and the space group belonged to be $P-1$. The anions and cations in **1** formed an alternating layered arrangement, while **2** crystallized in the monoclinic space group $P2_1/n$, and the anions and cations were arranged in columnar stacks. The temperature-dependent magnetic susceptibilities of salts **1** and **2** demonstrated spin chain magnetic exchange behavior.

Appendix A: Supplementary data

CCDC 2,023,007, 2,023,008, 2,063,630 and 2,063,631 contain the supplementary crystallographic data of **1** and **2**. These data can be obtained free of charge via http://www.ccdc.cam.ac.uk/conts/retrieving.html, or from the Cambridge Crystallographic Data Centre, 12 Union Road, Cambridge CB2 1EZ, UK; fax: (+44) 1223-336-033; or e-mail: deposit@ccdc.cam.ac.uk. Supplementary data associated with this article, including the IR spectra and PXRD results, can be found in the Supporting Information.

Supplementary Information The online version contains supplementary material available at https://doi.org/10.1007/s11243-021-00452-w.

Acknowledgements The authors thank the National Natural Science Foundation of China (Grant No. 21801218) and the Natural Science Foundation of the Jiangsu Higher Education Institutions of China (Grant No. 17KJB150040) for financial support.

References

1. Cassoux P, Valade L, Kobayashi H, Kobayashi A, Clark RA, Underhill AE (1991) Coord Chem Rev 110:115
2. Pullen AE, Olk R-M (1999) Coord Chem Rev 188:211
3. Robertson N, Cronin L (2002) Coord Chem Rev 227:93
4. Akutagawa T, Nakamura T (2000) Coord Chem Rev 198:297
5. Kato R (2004) Chem Rev 104:5319
6. Fourmigué M (2004) Acc Chem Res 37:179
7. Kobayashi A, Fujiwara E, Kobayashi H (2004) Chem Rev 104:5243
8. Bader K, Dengler D, Lenz S, Endeward B, Jiang SD, Neugebauer P, Slageren J (2014) Nat Commun 5:5304
9. Zadrozny JM, Niklas J, Poluektov OG, Freedman DE, Cent ACS (2015) Sci 1:488
10. Escalera-Moreno L, Suaud N, Gaita-Ariño A, Coronado E (2017) J Phys Chem Lett 8:1695
11. Hachem H, Cui HB, Tsumuraya T, Kato R, Jeannin O, Fourmigué M, Lorcy D (2020). J Mater Chem C. https://doi.org/10.1039/D0TC02868A
12. Hachem H, Jeannin O, Fourmigué M, Barrière F, Lorcy D (2020) Cryst Eng Commun 22:3579
13. Hachem H, Bellec N, Fourmigué M, Lorcy D (2020) Dalton Trans 49:6056
14. Duan HB, Ren XM, Meng QJ (2010) Coord Chem Rev 254:1509
15. Ren XM, Meng QJ, Song Y, Lu CS, Hu CJ, Chen XY (2002) Inorg Chem 41:5686
16. Ren XM, Okudera H, Kremer RK, Song Y, He C, Meng QJ, Wu PH (2004) Inorg Chem 43:2569
17. Ning WH, Zhai L, Liu JL, Ren XM, Ichihashi K, Nishihara S, Inoued K (2015) J Mater Chem C 3:7906
18. Yang H, Cheng T, Goddard WA, Ren XM (2019) J Phys Chem Lett 10:6432
19. Yuan GJ, Shao DS, Ren Q, Feng FY, Yang H, Wang L, Ren XM (1829) Cryst Growth Des 2020:20
20. Qian Y, Shao DS, Yao WW, Yao ZY, Wang L, Liu WL, Ren XM, Appl ACS (2020) Mater Interfaces 12:28129
21. Kusamoto T, Yamamoto HM, Tajima N, Oshima Y, Yamashita S, Kato R (2012) Inorg Chem 51:11645
22. Han YK, Seo DK, Kang H, Kang W, Noh DY (2004) Inorg Chem 43:7294
23. Mukai K, Senba N, Hatanaka T, Minakuchi H, Ohara K, Taniguchi M, Misaki Y, Hosokoshi Y, Inoue K, Azuma N (2004) Inorg Chem 43:566
24. Mukai K, Hatanaka T, Senba N, Nakayashiki T, Misaki Y, Tanaka K, Ueda K, Sugimoto T, Azuma N (2002) Inorg Chem 41:5066
25. Zang SQ, Ren XM, Su Y, Song Y, Tong W, Ni Z, Zhao H, Gao S, Meng Q (2009) Inorg Chem 48:9623
26. Zapata-Rivera J, Maynau D, Calzado CJ (2017) Chem Mater 29:4317
27. Kusamoto T, Yamamoto HM, Kato R (2013) Cryst Growth Des 13:4533
28. Kosaka Y, Yamamoto HM, Nakao A, Tamura M, Kato R (2007) J Am Chem Soc 129:3054
29. Lieffrig J, Jeannin O, Auban-Senzier P, Fourmigué M (2012) Inorg Chem 51:7144
30. Kusamoto T, Yamamoto HM, Tajima N, Oshima Y, Yamashita S, Kato R (2013) Inorg Chem 52:4759
31. Kato R, Cui HB, Tsumuraya T, Miyazaki T, Suzumura Y (2017) J Am Chem Soc 139(5):1770–1773
32. Akutagawa T, Nakamura T (2002) Coord Chem Rev 226:3
33. Akutagawa T, Nakamura T, Inabe T, Underhill AE (1998) Thin Solid Films 331:264
34. Hoshino N, Yoshii Y, Aonuma M, Kubo K, Nakamura T, Akutagawa T (2012) Inorg Chem 51:12968
35. Ye Q, Akutagawa T, Endo T, Noro S, Nakamura T, Xiong RG (2010) Inorg Chem 49:8591
36. Akutagawa T, Hasegawa T, Nakamura T, Inabe T (2002) J Am Chem Soc 124:8903
37. Akutagawa T, Shitagami K, Aonuma M, Noro S, Nakamura T (2009) Inorg Chem 48:4454
38. Akutagawa T, Shitagami K, Nishihara S, Takeda S, Hasegawa T, Nakamura T, Hosokoshi Y, Inoue K, Ikeuchi S, Miyazaki Y, Saito K (2005) J Am Chem Soc 127:4397
39. Ye Q, Akutagawa T, Hoshino N, Kikuchi T, Noro S, Xiong RG, Nakamura T (2011) Cryst Growth Des 11:4175
40. Ichihashi K, Konno D, Date T, Nishimura T, Maryunina KY, Inoue K, Nakaya T, Toyoda K, Tatewaki Y, Akutagawa T, Nakamura T, Nishihara S (2018) Chem Mater 30:7130
41. Ye Q, Shi PP, Fu XQ, Akutagawa T, Nakamura T (2013) Cryst Eng Commun 15:5307
42. Hiraga H, Miyasaka H, Clérac R, Fourmigué M, Yamashita M (2009) Inorg Chem 48:2887–2898
43. Takahashi K, Cui HB, Okano Y, Kobayashi H, Einaga Y, Sato O (2006) Inorg Chem 45:5739
44. Takahashi K, Cui HB, Okano Y, Kobayashi H, Mori H, Tajima H, Einaga Y, Sato O (2008) J Am Chem Soc 130:6688
45. Takahashi K, Mochida T, Sakurai T, Ohta H, Yamamoto T, Einaga Y, Mori H (1983) Angew Chem Int Ed 2014:53

46. Takahashi K, Moria H, Kobayashi H, Sato O (2019) Polyhedron 28:1776
47. Vieira BJC, Dias JC, Santos IC, Pereira LCJ, Gama VD, Waerenborgh JC (2015) Inorg Chem 54:1354
48. Okai M, Takahashi K, Sakurai T, Ohta H, Yamamoto T, Einaga Y (2015) J Mater Chem C 3:7858
49. Faulmann C, Szilágyi PÁ, Jacob K, Chahine J, Valade L (2009) New J Chem 33:1268
50. Chen Y, Cao F, Wei RM, Zhang Y, Zhang YQ, Song Y (2014) Dalton Trans 43:3783
51. Dorbes S, Valade L, Real JA, Faulmann C (2005) Chem Commun 1:69
52. Tejel C, Pomarede B, Legros JP, Valade L, Cassoux P, Ulmet JP (1989) Chem Mater 1:578
53. Cornelissen JP, Muller E, Vaassens PHS, Haasnoot JG, Reedijk J, Cassoux P (1992) Inorg Chem 31:2241
54. Fang Q, Thomas CWM, Zhou ZY, Yang QC, Liu Z, Yu WT, Zhu DB, Jiang MH (2002) J Chem Soc Dalton Trans 7:1377
55. Garreau B, Pomarède B, Cassoux P, Legros JP (1993) J Mater Chem 3:315
56. Pomarede B, Garreau B, Malfant I, Valade L, Cassoux P, Legros JP, Audouard A, Brossard L, Ulmet JP, Doublet ML, Canadell E (1994) Inorg Chem 33:3401
57. Yang H, Liu JL, Zhou LC, Ren XM (2014) Inorg Chem Front 1:426
58. Sun X, Yang H, Xu HY, Liu JL, Zhou LC, Ren XM (2015) Synth Metal 209:112
59. Yang H, An DY, Liu JL, Ren XM, Zhou LC, Wang HB (2015) RSC Adv 5:13857
60. Chen XR, Liu SX, Ren Q, Tian ZF, Huang XC, Wang L, Ren XM (2018) J Phys Chem B 122:12428
61. Davison A, Holm RH (1967) Inorg Synth 10:8
62. Chen XR, Xu XY, Huang XC, Ren FF, Wang J, Liu SX, Xue C, Tao JQ (2018) Polyhedron 147:55
63. Schläpfer CW, Nakamoto K (1975) Inorg Chem 14:1338
64. Bruker (2007) APEX 2, SAINT, XPREP. Bruker AXS Inc., Madison
65. Bruker (2001) SADABS. Bruker AXS Inc., Madison
66. Sheldrick GM (2014) SHELXS2014 and SHELXL2014. Program for the refinement of crystal structure. University of Göttingen, Germany
67. Lu T, Chen F (2012) Multiwfn a multifunctional wavefunction analyzer. J Comput Chem 33:580
68. Frisch MJ, Trucks GW, Schlegel HB, Scuseria GE, Robb MA, Cheeseman JR (2009) GAUSSIAN 09, Revision A.02. Gaussian Inc., Wallingford
69. Bonner J, Fisher ME (1964) Phys Rev 135:A640
70. Hall JW, Marsh WE, Weller RR, Hatfield WE (1981) Inorg Chem 20:1033
71. Kahn O (1993) Molecular magnetism. VCH Publishers Inc., New York, p 2

Publisher's Note Springer Nature remains neutral with regard to jurisdictional claims in published maps and institutional affiliations.